Dual roles of pearlite microstructure to interfere/facilitate gaseous hydrogen-assisted fatigue crack growth in plain carbon steels

Yuhei Ogawa[a,b], Haruki Nishida[c], Masami Nakamura[b,d], Vigdis Olden[e], Alexei Vinogradov[f], Hisao Matsunaga[a,b,g]

[a] Department of Mechanical Engineering, Kyushu University, 744 Motooka, Nishi-ku, Fukuoka 819-0395, Japan
[b] Research Center for Hydrogen Industrial Use and Storage (HYDROGENIUS), Kyushu University, 744 Motooka, Nishi-ku, Fukuoka 819-0395, Japan
[c] *Graduate School of Engineering, Kyushu University, 744 Motooka, Nishi-ku, Fukuoka 819-0395, J*apan
[d] Kobe Material Testing Laboratory Co., Ltd., 47-13 Niijima, Harima-cho, Kako-gun, Hyogo 675-0155, Japan
[e] SINTEF Industry, 7456 Trondheim, Norway
[f] Department of Mechanical and Industrial Engineering, Norwegian University of Science and Technology – NTNU, N-7491 Trondheim, Norway
[e] International Institute for Carbon-Neutral Energy Research (I2CNER), Kyushu University, 744 Motooka, Nishi-ku, Fukuoka 819-0395, Japan

Corresponding author: Yuhei Ogawa
E-mail: ogawa.yuhei.778@m.kyushu-u.ac.jp

Abstract

The fatigue crack growth behavior of two commercial carbon steels with different pearlite volume fractions was studied in a gaseous hydrogen environment. A positive impact of pearlite was accordingly identified to mitigate the hydrogen-assisted crack growth acceleration. This finding was ascribed to the ferrite/cementite lamellar structure aligned perpendicularly to the cracking direction, wherein the confronting cementite platelets functioned as the barriers to the propagating crack, resulting in intermittent arrest of the crack tip. Meanwhile, a brittle delamination fracture ensued in the lamellar lying parallel to the crack-plane, counteracting and partially diminishing the above positive aspect, especially when the pressure of hydrogen gas was high. The results of mechanical testing are discussed in light of fractographical and microstructural investigations of the crack wake.

Keywords: Fatigue crack growth, Carbon steel, Pearlite, Environmental effects, Hydrogen

1. Introduction

Hydrogen embrittlement (HE), which is commonly referred to as the mechanical degradation of metals due to hydrogen occlusion [1,2], has long been an obstacle against the rationale design of high-pressure hydrogen applications (*e.g.*, pressure vessels and pipelines for hydrogen storage and transportation). This phenomenon attracts an ever-increasing interest from materials scientists as well as from manufacturers fabricating the real industrial components. The effect of hydrogen on structural metals manifests itself straightforwardly as the reduction of strength/ductility in conventional tensile tests of smooth specimens [3,4], although its detrimental effect is apparent primarily in the form of the reduced resistance to the propagation of micro-cracks emanating from congenital stress-concentrators or microstructural inhomogeneities introduced in the course of plastic deformation [5,6]. Specifically, considering the components, *e.g*. gas vessels or pipelines, which are cyclically loaded owing to the repetitive gas pressurization/depressurization, the hydrogen impact on the fatigue performance of materials is a critical issue for ensuring their safety and reliability [7–9]. Hydrogen shortens the fatigue lives in gaseous environments as well as under electrochemical charging [8,10,11] due to accelerated propagation of fatigue cracks, the phenomenon known as hydrogen-assisted (HA-) fatigue crack growth (FCG) [7,12–14]. Since the primary materials for pressure vessels and pipelines are low-alloyed carbon steels with the ferrite-pearlite or tempered martensite microstructure, the vast research has been done on various aspects of the HA-FCG behavior in these two common types of microstructures [7,13,15–19]. In the present paper, we confine ourselves to ferrite-pearlite microstructures. The emphasis is placed on the role of pearlite grains in HA-FCG, which has not yet been precisely elucidated.

The previous works by the present authors were focused on the HA-FCG in pure polycrystalline ferrite, using α iron as a reference material [14,20,21]. The latently high susceptibility of ferrite to hydrogen was unveiled without any overlapping influence from other complex microstructural features. The FCG rate accelerated up to 30 times in hydrogen as compared with that measured in inert gas. The similar behavior observed in 0.16% low-carbon steel where the volume fraction of pearlite was low, and thereby, intra-ferrite fatigue cracking was a prevailing failure mode [15,16]. Meanwhile, a noteworthy result was reported by Ronevich et al., who investigated the HA-FCG behavior in pipeline X65 steel (0.08%C) with a banded ferrite-pearlite microstructure in 21 MPa hydrogen gas [17]. They uncovered an advantageous effect of pearlite which can mitigate the crack growth acceleration, yet the effect was limited only to the situation when the rolling bands of pearlite clusters were aligned perpendicularly to both of the crack-plane and the crack growing direction. The result was rationalized in light of the hard nature of pearlite [17]: it was unlikely for the crack to break through hard pearlite obstacles, giving rise to frequent deviations of the crack from the straight path, branching and the resultant stress shielding at the deflected crack-front [22]. A similar phenomenon has been found in the ferrite-pearlite microstructure even in vacuum *via in-situ* observation in a scanning electron microscope (SEM) [23]. These findings raise an expectation for the utilization of pearlite as a structural agent to improve the HA-FCG resistance of steels when it is viewed merely at an intergranular scale.

At smaller length-scales, an intrinsic HE-sensitivity of pearlite has been studied mainly on eutectoid steels, their cold-drawn rods or wires [24–28]. The progressive perceptions on their hydrogen diffusion/trapping properties [25,29–31] and the unique fracture characteristics attributed to the lamellar structure comprising soft ferrite and hard cementite (Fe_3C) are ongoingly reported [32–34]. In general, cold-drawn eutectoid steels appear to be notably less sensitive to HE despite their prominently high tensile strength [24,26,27]. This can be ascribed to the absence of prior-austenite grain boundaries and associating film-like carbide precipitates that act as one of the preferential HE initiation sites [24]. Besides, it has been suggested that axially-aligned cementite platelets suppress the lateral propagation of hydrogen-induced micro-cracks [26,27].

However, based on an atomistic simulation, McEniry et al. have recently inferred that pearlite can also be HE-sensitive because the ferrite/cementite coherent interfaces can serve as an energy "trough" for hydrogen atoms, eventually leading to the loss of the interface bonding force [35]. An independent experimental study by Tomatsu et al. has strongly corroborated predictions made by McEniry et al. [36]. In this work, micro-cantilever bending tests were performed where hydrogen was cathodically introduced into the miniaturized samples. It was found that interface delamination occurred when the planes of the crack and pearlite lamellar are mutually parallel, whereas the HE-crack transecting the lamellar remained to propagate at a low velocity comparable to that measured under the absence of hydrogen. It should be noted, however, that even if the lamellar alignment and loading axis are mutually parallel, HE fracture of pearlite can be enhanced when the inter-lamellar spacing of pearlite colonies is relatively large [37,38]. That is, an accelerated shear fracture of pearlite becomes another principal HE-mode, giving rise to a loss of ductility under uniaxial tensile loading as well as to a faster crack extension in notch tensile tests both accompanying fracture surface topography with evidence of the insistent lamellar shearing [33,34,37]. Thus, an important caution is that the hitherto-known superior HE-resistance of pearlite is not a permanent one but possibly breaks down due to the combination of loading mode and microstructural factors including (i) lamellar orientation and (ii) spacing. In the commercial hot-rolled carbon steels where these two microstructural factors naturally fall into random, a complex synergy of those positive and negative aspects of pearlite are inevitably expected. In this regard, the role of pearlite on the HA-FCG characteristics in the ferrite-pearlite mixed microstructure remains elusive and incomplete, thus to be clarified under a more systematically assembled experimental framework.

In this study, we prepared two types of commercial carbon steels that differed primarily by the carbon content. FCG tests were performed under a gaseous hydrogen environment to gain deeper insight into the HA-FCG behavior in steels with significantly distinct pearlite volume fractions. The colonies of ferrite/cementite lamellar in both the materials were randomly oriented while having an almost equivalent range of inter-lamellar spacings: a comparison of their behaviors enables to detect the net effects of pearlite under the possibility for the operation of all the above-mentioned feasible failure modes. Electron microscopy examinations of the crack-wake deformation substructures combined with detailed fractography were carried out to unveil the details of fatigue fracture mechanisms. The observations indirectly yet explicitly uncovered the dual roles played by pearlite to interfere/facilitate the HA-FCG. The competitive relationships of those counteracting effects as a function of hydrogen gas pressure are revealed and discussed in what follows.

2. Materials and Methods

2.1 Materials

The materials used were commercially-available, 32 mm-thick hot-rolled carbon steel plates designated as S25C and S55C in the Japanese Industrial Standard (JIS). The carbon contents were 0.25 and 0.54 mass %, respectively. The remaining chemical compositions and the tensile mechanical properties measured in ambient air are listed in Table 1. Although these two steels are, in practice, not used for the real hydrogen gas vessels and pipelines, their simple alloy constituent is superior than complex practical steels in an attempt to gain more insight into the net effect of pearlite.

Table 1 Chemical compositions (mass %) and tensile mechanical properties - lower yield stress, σ_{Ly} and ultimate tensile strength, σ_B (both in MPa), of the two materials used in this study.

Material	C	Si	Mn	P	S	Cu	Ni	Cr	σ_{Ly}	σ_B
S25C	0.25	0.16	0.46	0.016	0.003	0.01	0.01	0.01	252	464
S55C	0.54	0.17	0.62	0.014	0.01	0.12	0.06	0.09	289	615

Fig. 1 (a) and (b) present the optical images of the initial microstructures after etching with 3% nital solution. The white regions correspond to ferrite, while black areas denote pearlite which exhibits banded arrangements lying parallel to the rolling planes. The pearlite grain sizes of the two materials were both approximately 20~50 μm, although the ferrite grains were somewhat larger in S25C steel (20~40 μm) than those in S55C steel (10~20 μm). The ratio of pearlite was obviously greater in S55C owing simply to its higher carbon concentration. Provided that these ferrite-pearlite microstructures were generated *via* slow-cooling after the end of hot-rolling processes, relevant volume fractions of pearlite, f_p, can be estimated by the following equation, considering the lever rule between pro-eutectoid ferrite and austenite at the A_1 temperature [39].

$$f_p = \frac{C - 0.02}{0.77 - 0.02} \times 100\ [\%] \tag{1}$$

According to Eq. (1), the f_p of S25C and S55C steels were calculated to be 31 and 69%, respectively. In Fig. 1 (c) and (d), detailed SEM micrographs of the typical pearlite grains in the two materials are provided. Orientations of ferrite/cementite lamellar colonies are random; the inter-lamellar spacing ranges from 0.2 to 1.2 µm. Note also that the fraction of pearlite grains having the larger half of the above spacing range, *i.e.*, 0.6~1.2 µm, was slightly higher in S55C than in S25C.

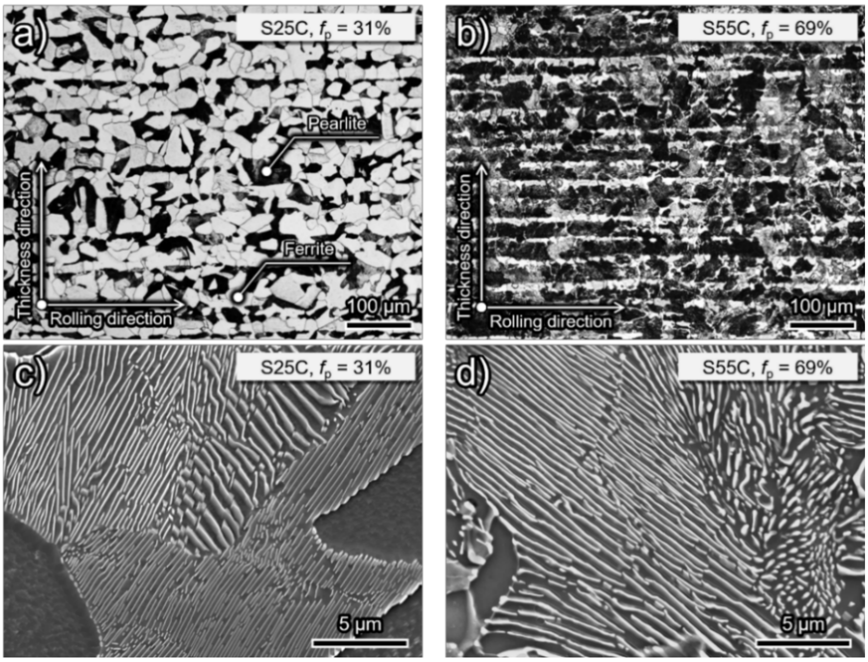

Fig. 1 Initial microstructures of (a)(c) S25C and (b)(d) S55C steels viewed on the L-T planes. (a) and (b) are optical micrographs after etching with 3% nital solution, while (c) and (d) present the magnified SEM images of the typical pearlite grains possessing ferrite-cementite lamellar structure.

2.2 Specimen configuration and test methodology

Compact-tension (CT) specimen with a width, W, of 50.8 mm and a thickness, B, of 10.0 mm was extracted from the plates so that its loading axis is parallel to the rolling direction and the crack grows toward the transverse direction (L-T orientation).

FCG experiments were performed according to the ASTM-E647 standard [40] under a constant load-range control (ΔP-constant tests), using a 100 kN load-capacity servo-hydraulic testing machine, which was attached to a 100 MPa pressure vessel. ΔP-constant tests provide the relationship between fatigue crack propagation distance per cycle, da/dN, and the stress intensity factor range, ΔK. The crack length was monitored by an elastic unloading compliance method using a clip-on gauge. The data were acquired in laboratory air as a reference environment as well as in 0.7 and 90 MPa hydrogen gas (purity of 99.999%) at room temperature (300 K) under load ratio, R = 0.1 and test frequency, f = 1 Hz. For more detailed information about the experimental methodology, the readers shall refer to the authors' previous papers [14,15,20]. After the tests, the CT specimens were broken into two parts by additional fatigue loading in air, and the fracture surfaces were observed by a field-emission scanning electron microscope (SEM, JEOL JSM-7F), operated at an acceleration voltage of 15 kV.

In addition to the ΔP-constant tests, FCG tests under ΔK-control (ΔK-constant tests) were performed in the same environmental conditions at $\Delta K = 25$ MPa·m$^{1/2}$ by continuously decreasing the load range as the length of fatigue crack increased; the R-value was kept constant at 0.1. Since the test frequency is one of the critical factors affecting the HA-FCG behavior (*i.e.*, the diffusion of hydrogen from the crack-tip may function as the rate-controlling process for fracture) [41–43], the FCG rates at this specific ΔK level were measured at three test frequencies; f = 0.01, 0.1 and 1 Hz. The specimens subjected to the tests were sliced along their mid-thickness sections and carefully polished with colloidal SiO_2 solution for ensuring damage-free surfaces. Electron backscattering diffraction (EBSD) and electron channeling contrast imaging (ECCI) [44] were employed to visualize the microstructural crack paths and the deformation substructures for the elucidation of detailed fracture mechanisms. The same SEM with the fractographic analysis was used, yet at acceleration voltages of 15 kV for EBSD and of 30 kV for ECCI. The electron beam step size for the EBSD was set as 50 nm.

3. Results

3.1 Macroscale fatigue crack growth characteristics

3.1.1 Overall trend

Fig. 2 depicts the relationships between da/dN and ΔK obtained in laboratory air as well as in a hydrogen gas environment with the pressures of 0.7 and 90 MPa. In the same diagrams, the properties of pure ferritic polycrystalline iron (grain size of 100~200 μm) [20] and of a 0.16%C steel (grain sizes of 20~30 μm and f_p = 19% according to Eq. (1)) [15] are plotted together for the sake of comparison, which were acquired using the CT specimen having an identical shape with the present experiments. The absence of da/dN-ΔK data of pure iron at the ΔK greater than 20 MPa·m$^{1/2}$ is due to the limitation by the small-scale-yielding requirement [40] that made the data acquisition unfeasible in such material with low yield strength.

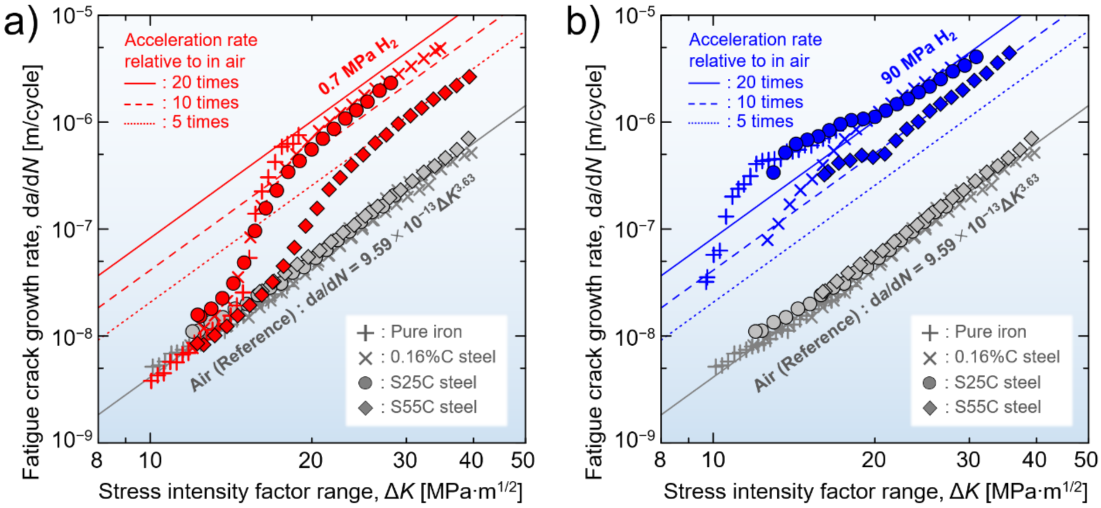

Fig. 2 Relationships between fatigue crack growth rate, da/dN, and stress intensity factor range, ΔK, of S25C and S55C steels in air as well as in (a) 0.7 and (b) 90 MPa hydrogen gas at room temperature. The data of pure ferritic iron [20] and 0.16%C steel [15] acquired in the authors' previous works are plotted together for comparison. All the data were acquired at f = 1 Hz except that for the test of 0.16%C steel in air wherein the testing frequency was set at 5 Hz.

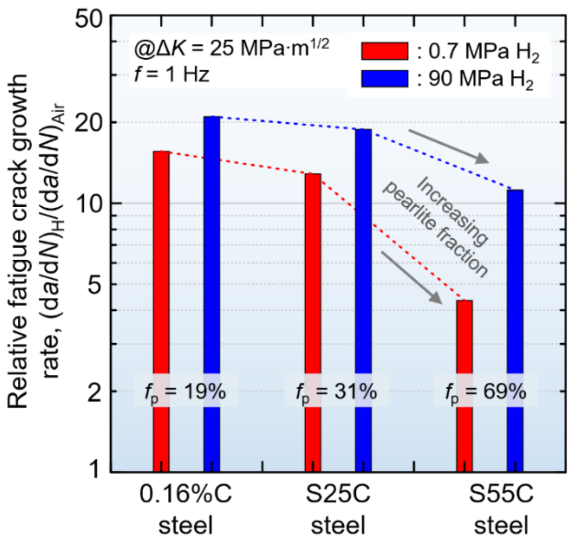

Fig. 3 Relative fatigue crack growth rate in hydrogen gas with respect to that in air, $(\mathrm{d}a/\mathrm{d}N)_{\mathrm{H}}/(\mathrm{d}a/\mathrm{d}N)_{\mathrm{Air}}$, of S25C and S55C steels as well as of 0.16%C steel [15] at ΔK = 25 MPa·m$^{1/2}$. The data were re-constructed from the da/dN-ΔK diagrams in Fig. 2.

For all specimens tested, the da/dN-ΔK curves in air converged into a narrow band with which a straight relationship was seen on the logarithmic diagram according to the Paris law. On the other hand, a dramatic enhancement of the FCG rate was seen in hydrogen gas. While the Paris behavior of the fatigue crack appeared to be insensitive to the microstructure in air as frequently reported for steels, the magnitude of the FCG acceleration in H-gas was found to be strongly dependent on the material, its microstructure, hydrogen gas pressure and ΔK. In 0.7 MPa hydrogen gas, a transitional behavior of the FCG acceleration was clearly seen. The da/dN values were not affected by hydrogen at low ΔK, followed by a sharp acceleration of the FCG rate at ΔK of 15~17 MPa·m$^{1/2}$. After the transition period, the da/dN-ΔK responses stabilized and fell into parallel lines with the Paris slope similar to that in air. In what follows, this stabilized regime of FCG will be discussed in detail. The behaviors in 90 MPa hydrogen gas were somewhat different from that at 0.7 MPa in that considerable FCG acceleration was observed already at $\Delta K < 15$ MPa·m$^{1/2}$ (with small humps of the da/dN-ΔK curves at $\Delta K = 10$~20 MPa·m$^{1/2}$), though the stabilized state of HA-FCG was eventually reached in response to the ΔK increase.

3.1.2 Significance of HA-FCG under the different pearlite volume fraction

In the materials with the carbon content smaller than 0.25% (*i.e.*, pure iron, 0.16%C steel and S25C steel), the mutual differences of da/dN in the stabilized state were minimal on the logarithmic ordinate, and the rate of FCG acceleration relative to in air came up around 10~20 times regardless of the pressures of hydrogen gas. Meanwhile, increasing the carbon content toward 0.54% explicitly mitigated the degree of FCG acceleration, and the significance of such suppression effect due to carbon alloying was more substantial at 0.7 MPa hydrogen gas than at 90 MPa. In Fig. 3, the FCG rates in hydrogen gas normalized by those in air, $(da/dN)_H/(da/dN)_{Air}$, at $\Delta K = 25$ MPa·m$^{1/2}$ are plotted for the three materials except for pure iron. Notably, 0.54% carbon ($f_p = 69\%$) reduced the $(da/dN)_H/(da/dN)_{Air}$ down to ≈ 11 in 90 MPa hydrogen gas from those of two other materials with $(da/dN)_H/(da/dN)_{Air} \approx$ 19~21. Besides, the impact was further evident at 0.7 MPa, wherein the $(da/dN)_H/(da/dN)_{Air}$ in S55C steel was merely < 5. It seems, at first glance, that the superior property of S55C than S25C owes its smaller ferrite grain size (see Fig. 1) since there has been a hitherto-known perception that the grain refinement is an effective way to improve the HE-resistance in many metallic materials [45,46]. Nonetheless, given that the presumption is valid, a controversy arises about the similarities among the FCG characteristics of pure iron, 0.16%C steel and S25C steel *viz.* the grain size of pure iron is almost an order of magnitude greater than the other two. Therefore, it is deemed that the grain size variation within a few tens to hundred micrometers range does not exert any sizeable impact in regard to the HA-FCG resistance. This allows supposing that the identified advantage of carbon alloying has its roots in the increased volume fraction of pearlite.

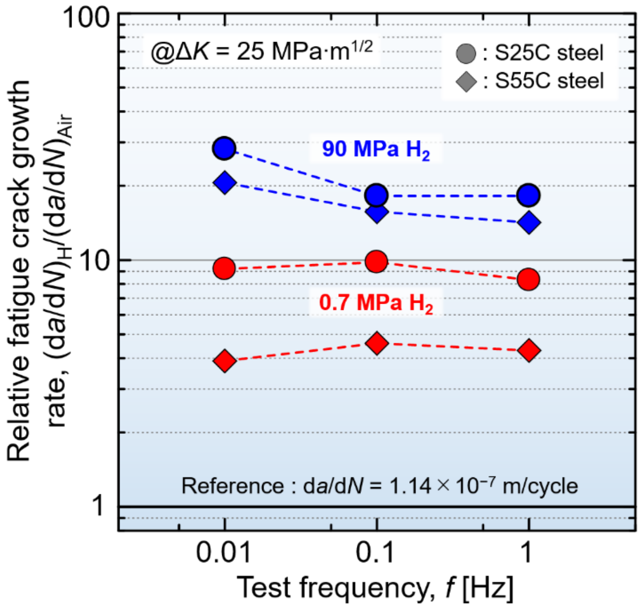

Fig. 4 Relative fatigue crack growth rate in hydrogen gas with respect to that in air, $(\mathrm{d}a/\mathrm{d}N)_{\mathrm{H}}/(\mathrm{d}a/\mathrm{d}N)_{\mathrm{Air}}$, of S25C and S55C steels at $\Delta K = 25$ MPa·m$^{1/2}$ as a function of test frequency, f.

3.1.3 Effect of the test frequency

Fig. 4 shows the $(\mathrm{d}a/\mathrm{d}N)_{\mathrm{H}}/(\mathrm{d}a/\mathrm{d}N)_{\mathrm{Air}}$ at $\Delta K = 25$ MPa·m$^{1/2}$ in 0.7 and 90 MPa hydrogen gas which were obtained *via* ΔK-constant tests under $f = 0.01$~1 Hz. In the materials in which the hydrogen infiltration from crack-tip is a rate-controlling process for fracture, $(\mathrm{d}a/\mathrm{d}N)_{\mathrm{H}}/(\mathrm{d}a/\mathrm{d}N)_{\mathrm{Air}}$ is enhanced with lowering f: an order of magnitude increase in $(\mathrm{d}a/\mathrm{d}N)_{\mathrm{H}}/(\mathrm{d}a/\mathrm{d}N)_{\mathrm{Air}}$ could be observed as f is decreased to one-tenth, for instance, from 1 Hz to 0.1 Hz [41–43,47]. Such a behavior is widely known as time-dependent HA-cracking, which is a classical phenomenon in high-strength martensitic steels with tensile strengths well exceeding 1 GPa. By contrast, $(\mathrm{d}a/\mathrm{d}N)_{\mathrm{H}}/(\mathrm{d}a/\mathrm{d}N)_{\mathrm{Air}}$ in S25C and S55C steels exhibited only a weak dependence on f within the presently-examined frequency range, indicating that the distance of crack propagation is primarily determined by the number of applied load cycles and is not affected by the load-holding time. Similar cycle-dependent behavior of HA-FCG has been reported in ferrite-based carbon steels as well as in austenitic stainless steels in the previous studies by the authors' research group [12,15]. The most intriguing finding in Fig. 4 is that S55C steel persistently exhibited remarkably slower FCG rates than S25C steel when compared at the same hydrogen gas pressure. This indicates that the superiority of greater carbon-content (pearlite-rich) materials from a perspective of HA-FCG resistance is still active even at the low-frequency regime, which is of practical importance in an attempt to utilize them in real high-pressure hydrogen gas applications.

3.2 Fractography

3.2.1 Fracture surfaces in a reference environment

The fracture surface images of the two materials tested at ΔP-constant in laboratory air have been observed at the crack length corresponding to at ΔK = 25 MPa·m$^{1/2}$, and are depicted in Fig. 5. All fractographic images were obtained at the near-mid-thickness part of the CT specimens. These images reveal that the overall fracture surfaces of both materials are topologically intricate (Fig. 5 (a) and (b)), indicating ductile and sluggish crack propagation, whereas diverse microscopic morphological components are observed at higher magnifications (Fig. 5 (c) and (d)). In S25C steel with f_p = 31%, the primary surface feature of interest is represented by typical ductile fatigue striations as shown in Fig. 5 (c). These striations are oriented perpendicularly to the crack growth direction and are regularly ordered so that the inter-striations spacings were reasonably consistent with the experimentally-measured macroscopic FCG rate (da/dN ≈ 10^{-7} m/cycle at ΔK = 25 MPa·m$^{1/2}$ (Fig. 2)). Although similar fatigue striations were occasionally found, another type of striated pattern dominated the fracture surface profile in S55C steel with f_p = 69% (see Fig. 5 (d) for details). Unlike the conventional fatigue striations shown in Fig. 5 (c), the second type striations observed in S55C steel have greater spacings (~500 nm) and are not arranged along a specific direction. The inset in Fig. 5 (d) shows a magnified view of the region surrounded by a white dashed rectangle, demonstrating that those striations are microscopically composed of the successive step-wise or sometimes hill-and-valley-like configurations. At the center of each step or the tops/bottoms of the hills/valleys, the embedded cementite platelets stick out and can be seen as thin strips with a thickness of approximately 100 nm (marked by white arrows). Thus, it can be inferred that this feature bears its origin from the tearing of pearlite lamellar aligned vertically to the crack-plane (Pearlite tearing, PT). This will be discussed deeper on the basis of the crack-wake observations in Section 3.3.

3.2.2 Fracture surfaces in hydrogen gas

Figure 6 and Fig. 7 present the fracture surfaces of S25C and S55C steels tested in 0.7 and 90 MPa hydrogen gas at the same ΔK level as that in Fig. 5 (ΔK = 25 MPa·m$^{1/2}$) and at f = 1 Hz. One can notice that under the presence of hydrogen, ductile fatigue striations, which are common in air, were completely absent. Instead, the predominant surface morphology feature for S25C steel is seen as relatively flat planar regions, which are recognizable as the areas with dark contrast in the low magnification images (Fig. 6 (a) and (b)). The same distinct feature has been frequently reported in statically- as well as dynamically-loaded pure iron and various low-alloy steels and is commonly known as quasi-cleavage (QC), representing the HE-fracture of ferrite [5,20,48,49]. Occasionally, QC regions were superposed by brittle-like shallow striations (Fig. 6 (c)) with the spacings of an order of magnitude greater than those for the normal ductile striations observed at the same ΔK (Fig. 5 (c)), *i.e.*, conforming to the global FCG rate in hydrogen gas (Fig. 2). They were also frequently accompanied by river-like tear ridges parallel to the crack growth direction (Fig. 6(d)). The emergence of the last feature was particularly pronounced when the pressure of hydrogen gas was high.

The QC relief also appeared in S55C steel, albeit the QC area fraction was obviously smaller as compared with that in S25C steel owing simply to the lower volume content of ferrite (Fig. 7 (a) and (b)). The PT mechanism is still apparent in 0.7 MPa hydrogen gas, and its microscopic morphology (Fig. 7 (c)) does not substantially differ from that found in air (Fig. 5 (d)). However, the feature, which might not be very obvious in Fig. 7 (a), becomes very clear at 90 MPa (cf. Fig. 7 (d)) - that is extremely planer facets lying parallel or slightly inclined to the global crack-plane. Note that these facets were also noticeable at 0.7 MPa, although their area fraction increased sharply and reached ~20% at 90 MPa. Interestingly, around the periphery of the facets, numerous crevasse-like secondary cracks penetrating vertically to the global crack-plane and lying nearly along the crack growth direction were observed. The similarity of these planar and straight configurations of the facets and secondary cracks indicates that the two simultaneously-appearing fractographic features stemmed from the same origin in the materials microstructure.

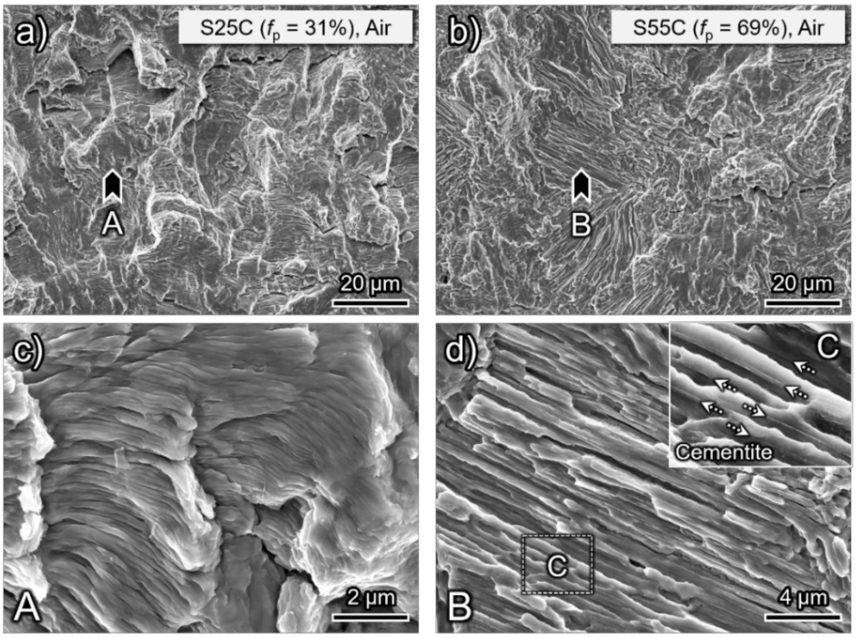

Fig. 5 SEM fractographs of (a)(c) S25C and (b)(d) S55C steels in laboratory air under ΔK = 25 $\mathrm{MPa \cdot m^{1/2}}$. (c) and (d) are the details of the regions marked with arrowheads in (a) and (b) respectively, besides the inset in (c) magnifies the area enclosed by a white dashed rectangle. The crack growth direction is from bottom to top in all the images.

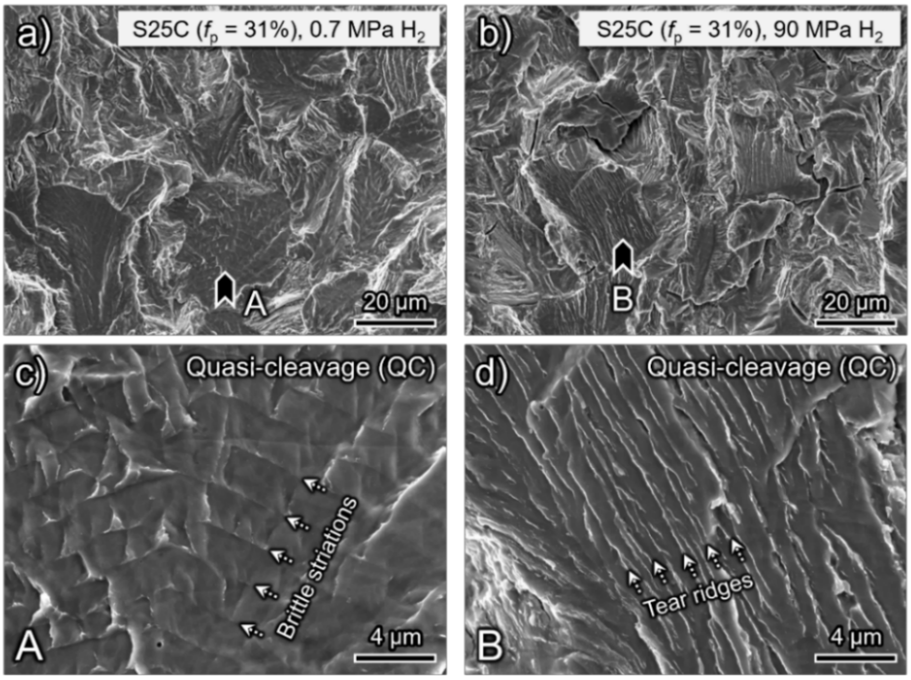

Fig. 6 SEM fractographs of S25C steel in (a)(c) 0.7 and (b)(d) 90 MPa hydrogen gas under the loading condition of ΔK = 25 MPa·m$^{1/2}$ and f = 1 Hz. (c) and (d) are the magnifications of the parts marked by arrowheads in (a) and (b), respectively. The crack growth direction is from bottom to top.

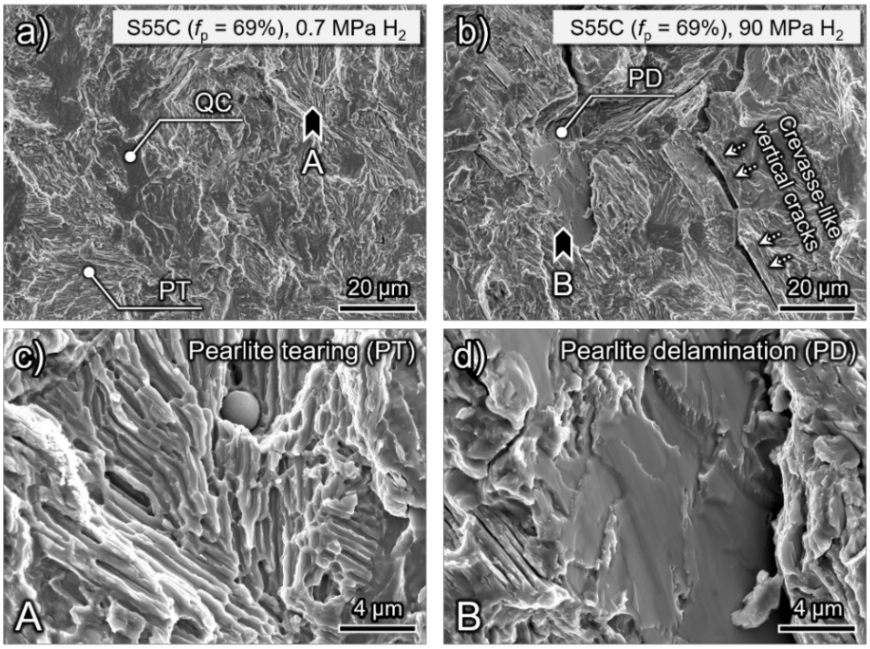

Fig. 7 SEM fractographs of S55C steel in (a)(c) 0.7 and (b)(d) 90 MPa hydrogen gas under the loading condition of ΔK = 25 MPa·m$^{1/2}$ and f = 1 Hz. (c) and (d) are the magnifications of the parts marked by arrowheads in (a) and (b), respectively. The crack growth direction is from bottom to top.

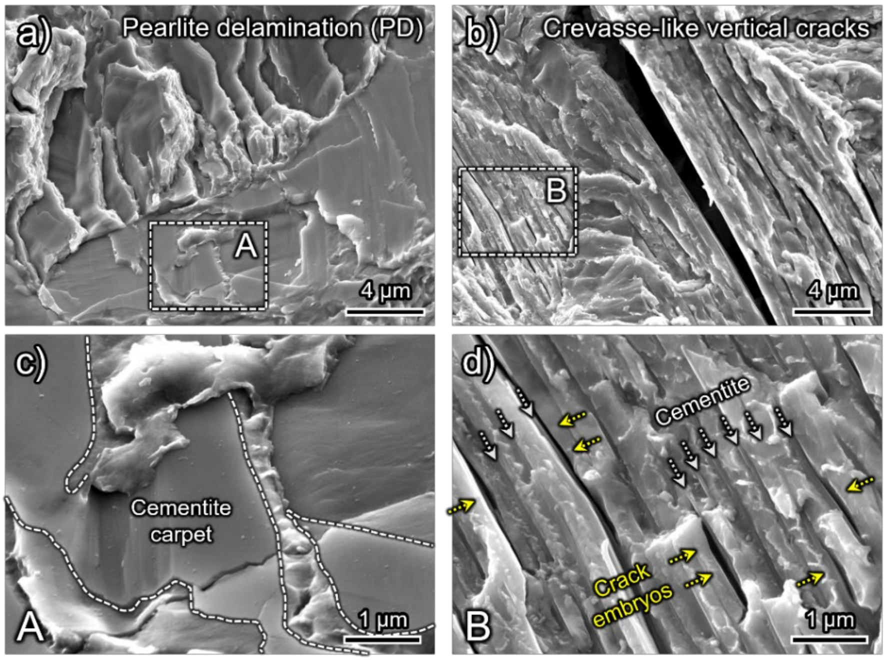

Fig. 8 (a)(c) another example of the planar facets similar to Fig. 7 (d), and (b)(d) the detailed view around the secondary crevasse-like crack marked by white arrows in Fig. 7 (b). (c) and (d) magnify the areas enclosed by white dashed rectangles in (a) and (b), respectively, and the crack growth direction is from bottom to top.

Figure 8 shows another example of the planar facet (Fig. 8 (a)) as well as the detailed view of a secondary crevasse-like crack (Fig. 8 (b)), in which the latter replicates the one marked by white arrows in Fig. 7 (b). The facets comprised successive step-and-terraces (Fig. 8 (a)), and the terrace segments were seemingly overlaid by carpets of the broad cementite platelets (Fig. 8 (c)). Furthermore, even at the position immediately adjacent to the large crevasse-like crack (Fig. 8 (d)), the lamellar-shaped fracture surface similar to that shown in Fig. 5 (d), *i.e.*, the PT pattern, was identified. These two facts demonstrate that the crevasse-like cracks, in conjunction with the planer facets, explicitly have their origin from the crack propagation across pearlite. The careful observation of Fig. 8 (d) reveals the presence of parallelly aligned clusters of tiny vertical cracks (marked by yellow arrows), which was hardly the case in air (Fig. 5 (d)) and in 0.7 MPa hydrogen gas (Fig. 7 (c)). Each of these embryonic vertical cracks was initiated along the interfaces between cementite platelets and inner pearlitic-ferrite layers, possibly reflecting their midway to eventually grow into sizable crevasse-like cracks such as the one depicted in Fig. 8 (b). An analogical failure process, *i.e.*, ferrite/cementite interface separation (Pearlite delamination, PD), may also be applied to the formation process of the faceted distinctions in Fig. 7 (d) and Fig. 8 (a). The condition determining whether the PD-type fracture emerges in the form of planar facets (Fig. 8 (a)) or crevasse-like cracks (Fig. 8 (b)) might be due to whether the stacking direction of the pearlite colonies locating at the crack-tip incidentally is nearly perpendicular or parallel to the global crack-plane. Supposedly, the driving force for triggering the crevasse-like cracking is the dilatational cyclic stress component acting in the thickness direction of CT specimens since our observations were done at mid-thickness parts where plane-strain stress state prevails [50]. However, because these secondary vertical cracks might have less influence than the planer facets in moving the Mode-I crack-front forward, the discussion regarding the PD-type fracture will only be based on the planar facets.

3.3 Microstructural fracture pathway and plasticity evolution around the crack-wake

3.3.1 Crack propagation modes in ferrite

In order to elucidate the selective microstructural fracture pathways in different materials and test environments as well as to connect them to the fractographic features presented in Section 3.2, the mid-thickness crack-wakes of the CT specimens subjected to ΔK-constant tests (ΔK = 25 MPa·m$^{1/2}$) were analyzed *via* EBSD and ECCI techniques. Figure 9 shows the results for S25C steel in terms of the EBSD-crystallographic orientation maps presented in inverse pole figure (IPF) colors (Fig. 9 (a)~(c)), as well as the kernel average misorientation (KAM) maps of some specific regions (Fig. 9 (d)~(f)) that were constructed using the data comprising third nearest neighbors around each hexagonal scan point. In these EBSD micrographs, a sole material phase selected for scanning is α iron and the data points with the confidence index smaller than 0.2 are omitted from the analysis. Thus, the cracks and the cementite phase are visualized in black color.

In the case of laboratory air, the transgranular fracture prevails so that the crack tends to propagate through ferrite, with only a minor part of the fracture path occurring across pearlite colonies (Fig. 9 (a)). The crack in ferrite grains exhibited a wavy shape. Substantial crystal rotation is seen in the crack vicinity (visible as the successive color changes in the IPF map), meaning that significant plasticity was involved during the FCG process. A consequence of the heavy plastic deformation can be recognized more straightforwardly in the KAM map (Fig. 9 (d)) wherein the network-like distribution of local misorientation amounting to a few degrees is evident. The ECCI micrograph of the same region (Fig. 11 (a)) revealed an ensemble structure of refined, equiaxed sub-grains, each of which possessed a micrometer-scale diameter, sharp boundaries and low dislocation density inside. This fact indicates that the KAM network detected in Fig. 9 (d) is also delineating the low-angle grain boundaries dividing these individual sub-grains.

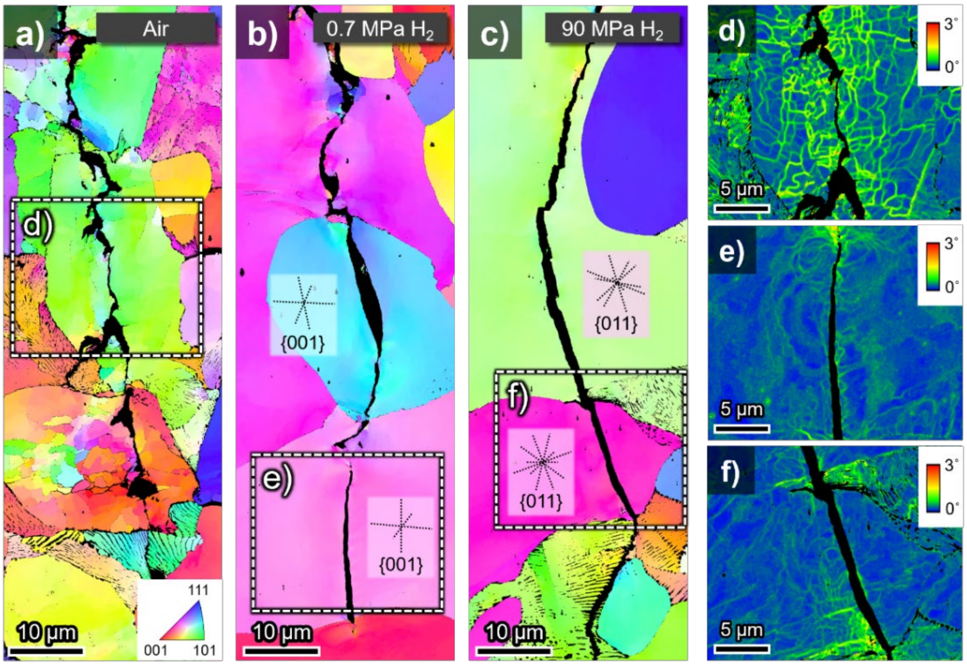

Fig. 9 Mid-thickness fracture paths of S25C steel tested in (a)(d) air, (b)(e) 0.7 MPa as well as (c)(f) 90 MPa hydrogen gas at ΔK = 25 MPa·m$^{1/2}$ and f = 1 Hz. (a)~(c) are the crystallographic orientation (IPF) maps, while (d)~(f) are the KAM maps of the regions surrounded by dashed rectangles in (a)~(c) respectively. The crack growth direction is from top to bottom.

Although the crack propagation across ferrite was predominant even in hydrogen gas, a distinct crack morphology was found, cf. Fig. 9 (a) in air and (b)-(c) in H-atmosphere. Compared to that in air, the crack path in H gas becomes less tortuous. Even though the crack path is not ideally straight and the wavy crack path can still be seen in the presence of hydrogen, the "wavelength" of the crack shape is notably greater than in air and tends to increase with hydrogen pressure. Besides, crack branching, and crumb formation occur much less frequently in H gas. Figure 9 (e) and (f) shows the typical KAM maps for the areas encompassing the vicinity of straight fragments of the fracture paths observed in hydrogen gas at 0.7 and 90 MPa, respectively. The critical difference from the deformation microstructures observed in air was that the regions with high KAM values as well as their network distributions were no longer seen along the crack path in H. Accordingly, the ECCI analysis of the same areas has no longer confirmed the presence of sub-grains; instead, the substructure was represented by loosely-developed dislocation cells (Fig. 11 (b) and (c)), implying a considerably lower level of the crack-wake plasticity evolution. The trace analysis on the two-dimensional cross-sections by EBSD revealed that the straight crack paths insistently followed {001} (*i.e.*, the cleavage plane) or {011} low-index planes of the body-centered cubic (BCC) crystal (Fig. 9 (b) and (c)).

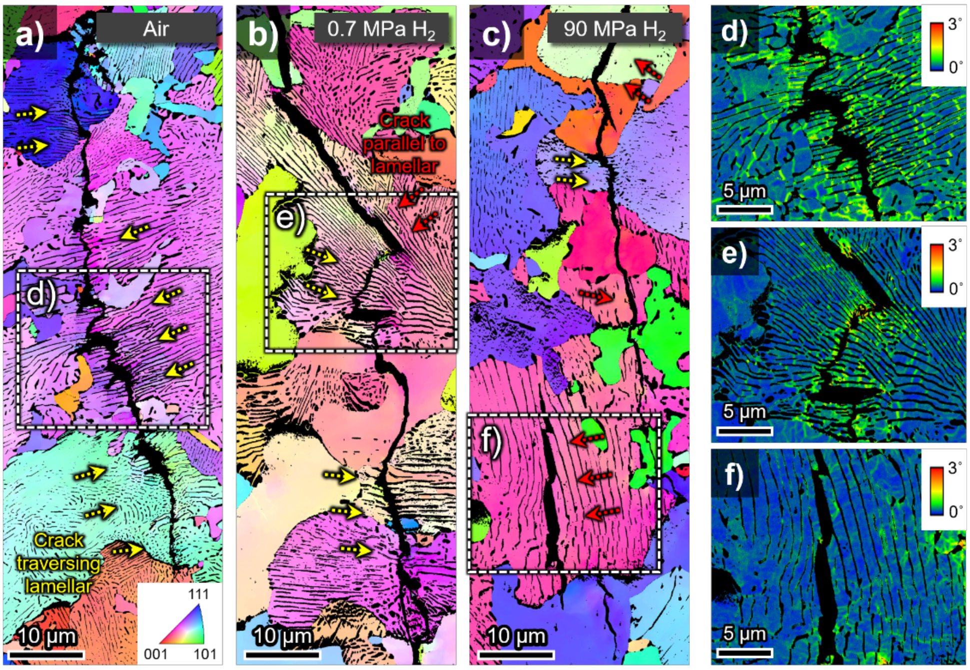

Fig. 10 Mid-thickness fracture paths of S55C steel tested in (a)(d) air, (b)(e) 0.7 MPa as well as (c)(f) 90 MPa hydrogen gas at ΔK = 25 MPa·m$^{1/2}$ and f = 1 Hz. (a)~(c) are the crystallographic orientation (IPF) maps, while (d)~(f) are the KAM maps of the regions surrounded by dashed rectangles in (a)~(c) respectively. The crack growth direction is from top to bottom.

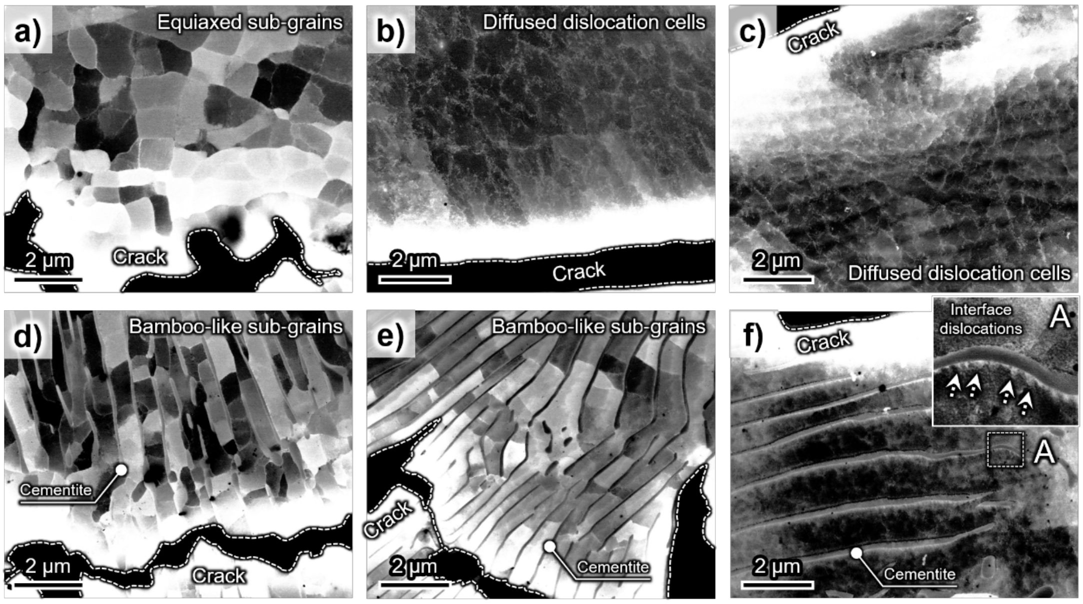

Fig. 11 ECCI micrographs of the deformation substructures adjacent to the crack propagation paths through (a)~(c) ferrite grains in S25C steel and (d)~(f) pearlite grains in S55C steel tested in (a)(d) air (b)(e) 0.7 MPa as well as (c)(f) 90 MPa hydrogen gas at ΔK = 25 MPa·m$^{1/2}$ and f = 1 Hz. (a)~(c) and (d)~(f) correspond to the same regions with Fig. 9 (d)~(f) and Fig. 10 (d)~(f) respectively. The inset in (f) magnifies the area enclosed by white rectangle A. The crack growth direction is from left to right.

3.3.2 Crack propagation modes in pearlite

With the increasing volume fraction of pearlite, f_p from 31 to 69%, the proportion of cracking pathway that passes through the pearlite grains reasonably increased in S55C steel; the IPF maps of the typical regions shown in Fig. 10 (a)~(c) highlight such a behavior. It is seen from Fig. 10 (a) that the pearlite-penetrating crack in air tends to propagate mainly through the ferrite/cementite lamellar aligned nearly perpendicularly to the crack growth direction (marked by yellow arrows), which yields notably high KAM values around its proximity (Fig. 10 (d)), resembling those shown in Fig. 9 (d). Let us notice, however, that the arrangement of these high KAM value data points was no longer similar to the cellular distribution shown in Fig. 9 (d). In the pearlitic regions of S55C steel, the KAM patterns appear in the ladder rung-like form bridging between the props consist of cementite platelets. Figure 11 (d) presents the ECCI image of the same region as that in Fig. 10 (d). The origin of the ladder-looking KAM distribution becomes evident: nearly equidistantly spaced parallel sub-boundaries form the bamboo-like sub-grains structure in the inter-cementite regions. Other characteristics of the sub-grains (such as sharp sub-boundaries and low internal dislocation density) do not differ appreciably from those observed in S25C steel (cf. Fig. 11 (a)). Moreover, another noteworthy fact following from Fig. 11 (d) is that the edge geometry of the crack exhibited a microscopically bumpy shape with the wave length of approximately the same order with the inter-lamellar spacing of pearlite captured in the micrograph. Based on these findings, we suggest that the striated feature appeared on the fracture surface (*i.e.*, the PT pattern (Fig. 5 (d)) as a consequence of this pearlite-transecting cracking mode. The underlying microscale process might involve fibrous tearing of pearlite lamellar comprising the fragmentation of cementite platelets and subsequent splitting off of pearlitic-ferrite in the close proximity of the crack-tip (its schematic illustration will be described in Fig. 12 (a)).

Considering the fracture behaviors in a pressurized hydrogen gas environment, one can notice that the crack propagation transecting the pearlite lamellar was still in operation to some extent, which was in good agreement with the presence of PT patterns on the fracture surface (Fig. 7 (c)). Nonetheless, another cracking mode came into stage and became indisputably more pronounced with the increasing hydrogen gas pressure from 0.7 to 90 MPa: the interlamellar crack path prevailed under these conditions as marked by red arrows in Fig. 10 (b) and (c). The preponderance of this mode of crack growth is nicely reflected by the planer facets on the fracture surfaces (*i.e.*, PD patterns seen in Figs. 7 (d) and 8 (a) discussed above) originating from the delamination along ferrite/cementite interfaces. Figure 10 (c) illustrates that the lower-half of the crack (*i.e.*, the part enclosed by the white dashed rectangle) is clearly disconnected from the relevant upper-half, although the two-dimensional observation is not suitable to reveal whether they were really isolated each other or actually connected in the sub-surface region of the sample. Fig. 10 (e) and Fig. 11 (e) magnify the examples of the PT-fractured portion in 0.7 MPa hydrogen gas, revealing that the ladder-looking KAM distribution and bamboo-like sub-grain structures similarly manifest, yet the extension of such region with high-KAM values from the crack contour seemed to be narrower than that in air (Fig. 10 (d)). Nevertheless, what should be additionally emphasized here is that the area surrounding PD in 90 MPa hydrogen gas showed little development of KAM (Fig. 10 (f)), and the corresponding ECCI (Fig. 11 (f)) revealed a complete absence of any evolved substructures in sub-grains or dislocation cells. A sole characteristic of the deformation microstructure around the PD was the regularly-spaced spike-like white contrast at the ferrite/cementite phase boundaries, as shown in the inset in Fig. 11 (f), for example. These contrast changes in the ECCI image are mainly due to the local elastic lattice distortion [44], which might be derived by the presence of interfacial dislocations accumulated in the course of deformation at the crack-tip volume.

4. Discussion

4.1 Summary of main results

In the two plain-carbon steels used for this investigation, an accelerated FCG relative to the normal rate in air was evident in gaseous hydrogen environment (Fig. 2), albeit to a different extent depending on the gas pressure. Under hydrogen-stimulated accelerated FCG, QC-type fracture prevailed (Fig. 6 and 7). The appearance of QC facets was quite similar to that reported for HE of iron and steels with ferrite-dominating microstructures [5,20,48,49]. The area fraction of QC in S25C steel eminently exceeded that in S55C steel. This fact indirectly yet certainly demonstrates that the QC facets found in the present study also reflect the propagation of HA-cracks across ferrite, potentially corresponding to the fracture along {001} or {011} planes detected in the crack-wake analysis by the EBSD characterization (Fig. 9 (b) and (c)). Thus far, the HA-cracking parallel to {001} and {011} planes of BCC crystal has been elaborated [20,51–53], and various fundamental hypotheses were proposed including the localization of ductile fracture [51], microscale cleavage owing to the locking of dislocations at the crack-tip [20], etc. Whatever the case is, an indisputable consequence is that the ferrite-QC mechanism is a root cause for the accelerated FCG, although the description regarding its underlying mechanisms is beyond the scope of this paper.

The present results for FCG in different materials align well with the numerus reports claiming that for many classes of materials microstructure has negligible effect on FCGR in Paris regime: the

FCG data for pure iron, 0.16%C steel and S25C and S55C steels fall on the same master line, when tested in air. Testing in hydrogen gas breaks this trend, and highlights the significance of the microstructure for the FCG under HE conditions, depending on gas pressure. The main thrust of the present work was to show that an introduction of high-volume fraction of pearlite into ferrite microstructure mitigates the FCG acceleration in hydrogen (Fig. 3), see Section 3.1.2. The impact was more prominent when the pressure of hydrogen gas was low, *i.e.*, 0.7 MPa, yet it was nonetheless appreciable at an extremely high-pressure up to 90 MPa too. When attempting to rationalize the cause of this HA-FCG suppression effect, the difference in hydrogen diffusivity in ferrite and pearlite [29,35,54] should firstly be considered since the presence of various trapping sites in pearlite hinders the lattice diffusion of hydrogen [25,29,37,54]. Therefore, the hydrogen supply towards the crack-tip fracture process zone is retarded. However, our ΔK-constant tests with the frequency varied within 0.01~1 Hz revealed no significant frequency dependence of the FCG acceleration rate irrespectively of f_p (Fig. 4). This finding implies that some sort of intrinsic microstructural aspect of pearlite is more important than the simple diffusivity alteration for the onset of the HA-FCG suppression effect, albeit the possible trivial influence arising from the diffusion kinetics cannot be completely excluded based merely on the present experiments.

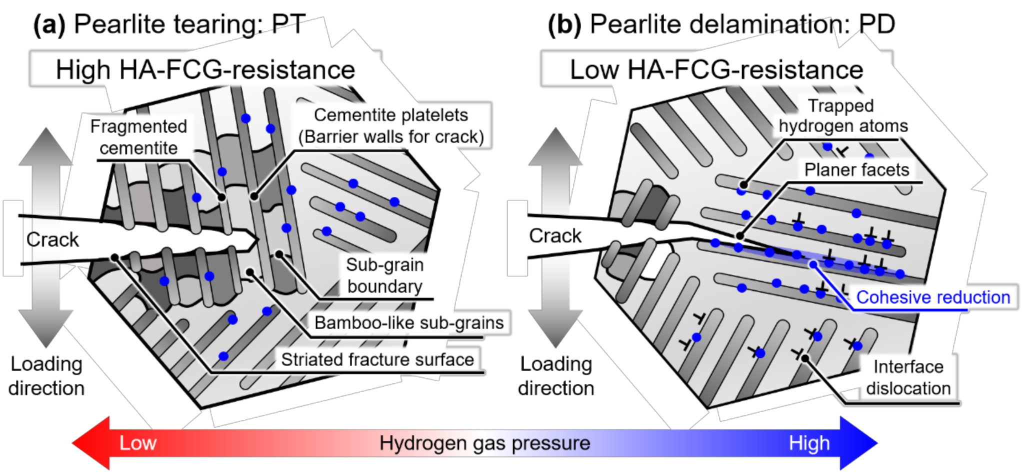

Fig. 12 Schematic illustrations of the two fatigue crack propagation modes through pearlite grains under the presence of gaseous hydrogen. (a) describes the cracking-mode transecting ferrite/cementite lamellar aligned nearly perpendicular to the crack-plane (pearlite tearing, PT), wherein confronting cementite platelets function as barrier walls for slowing down the crack. Well-evolved sub-grain structure is thus developed around the crack-wake owing to the high level of cumulative plastic strain. Meanwhile, (b) denotes the delamination-type fracture along the ferrite/cementite interfaces lying almost parallel to the crack-plane (pearlite delamination, PD). Hydrogen atoms occluded from the crack-tip are effectively trapped at the phase boundaries that are decorated by interface dislocations, thereby making the interface debonding easier according to the hydrogen-enhanced decohesion (HEDE) hypothesis. The PD type fracture becomes particularly pronounced as the pressure of hydrogen gas is increased.

Steel microstructure influences the fatigue crack behavior primarily by changing the mode of crack growth. During propagation, the fatigue crack advances incrementally along the crack plane through ferritic and pearlitic phases interchangeably. While the crack encountering pearlitic lamellae, two distinct failure modes were clearly found out (Sections 3.2.2 to 3.3.2): the crack propagation transecting the ferrite/cementite lamellar aligned nearly perpendicular to the crack-plane (*i.e*., PT-type fracture (Fig. 5 (d), Fig. 7 (c) and Fig. 10 (b)) and the delamination type cracking in the lamellar structure almost lying parallel to the crack-plane (*i.e*., PD-type fracture (Fig. 7 (d) and Fig. 10 (c))); their schematic illustrations are provided in Fig. 12. The PT mechanism showed up commonly both in air and hydrogen gas, while PD was specific to the hydrogen effect and became more pronounced at the higher hydrogen pressure. Combining this outcome with the fact that the positive impact of pearlite was more pronounced at the lower gas pressure (Fig. 3), one can come up with a hypothesis that the HA-FCG suppression effect by pearlite is related the PT-type of cracking. As opposes to this, the PD mode has no beneficial aspects but rather adversely contributes to the FCG acceleration and partially compromises the retardation effect of PT on FCG. The most marked difference between the two representative fracture modes was seen in the evolution of KAM levels and in the underlying dislocation substructures in the crack wake (Fig. 10 and Fig. 11 (d)~(f)). A key to establish the above hypothesis may lie in these findings, as a plausible explanation will be given hereafter. In addition, the different role played by pearlite in the fracture behavior during FCG and conventional monotonic tensile testing will also be highlighted and argued in the context of forthcoming discussion.

4.2 Crack-wake substructure evolution as an indirect tool to measure the FCG rate

The evolution process of dislocation substructures and their resultant spatial arrangement in the volume enclosing fatigue crack-tip has been studied in many metals, including iron [55], copper [56], aluminum [57] and many others, using transmission electron microscopy. Besides, it was also substantiated by the authors' previous ECCI characterizations of pure iron and 0.16%C steel [14,16,20]. On one level or another, the consensus exists that the dislocations tend to be sparsely distributed far away from the crack, while they naturally form more complex self-organized configurations in the proximity of the crack tip [58–60]. In view of existing strain gradients ahead of the crack tip, this behavior can be plausibly rationalized as follows. Consider a fixed inspection volume located on the extension line of propagating fatigue crack and considers the deformation sequence in its inward during the process of the crack-tip to gradually approach and finally passes through it. When the cyclic plastic zone reaches this volume of interest, it starts yielding, and dislocations are initially introduced in the form of discrete loops or planar arrays. As the crack get closer, the cyclic plastic strain amplitude increases to the inspection volume, giving rise to typical cyclically induced series of local transformations of randomly arranged dislocations to tangles, dipolar bundles (veins), walls and, finally, cells when the strain amplitude is large enough. Upon the contact of the crack-tip and the inspection volume, the cumulative strain climaxes and encourages the readily pre-formed cell walls to grow sharper and to increase the transverse misorientation angles through the annihilation of unlike dislocations and re-distribution of the excess dislocations of the same sign within cell walls [56,57,61]. As a consequence of this deformation sequence, the well-developed and mutually-misoriented sub-grains are left behind the crack-wake after the crack-tip passage, in a way similar to the grain sub-division *via* dynamic recovery brought about by the large multiaxial strains at the crack tip [14,16,56,57]. Ultimately, the evolutional state of the dislocation substructures in the vicinity of the fatigue crack qualitatively follows the magnitude and the cumulation of plastic strain (*i.e.*, strain histories) applied to the material embraced inside the cyclic plastic zone (CPZ). In this context, examining the KAM and/or ECCIs on the crack-wakes of the specimens tested in different environment potentially provides an indirect measure of the difference in FCG rate, when the comparison is made under an identical ΔK and same microstructural feature in which equivalence of the applied plastic strain amplitude is ensured.

4.3 Substructure evolution in the presence of hydrogen

Rice established a method for estimating the size of CPZ, r_c formed in front of the fatigue crack-tip and proposed the following equation as a function of yield stress, σ_y and the maximum stress intensity factor range, K_{max} [62]:

$$r_c = \frac{\pi}{8}\left(\frac{K_{max}}{2\sigma_y}\right)^2 \quad (2)$$

According to Eq. (2) and expediently substituting σ_y with the σ_{Ly} in Table 1, the r_c of S25C steel at ΔK = 25 MPa·m$^{1/2}$ (K_{max} = 27.8 MPa·m$^{1/2}$ at R = 0.1) is calculated to be ≈1.2 mm. This means that more than 10000 cycles were required for the crack in air to propagate through the pre-existing CPZ ahead of its tip (recall that da/d$N \approx 10^{-7}$ m/cycle at ΔK = 25 MPa·m$^{1/2}$ (Fig. 2)). The accumulation of plastic strain in the course of such a process is reflected by the well-organized sub-grain structure shown in Fig. 9 (d). On the other hand, the structures representing a halfway to evolving into sub-grains, *i.e.*, dislocation cells, was a predominant feature in the proximity of the cracks running parallel to {001} or {011} planes of ferrite in hydrogen gas (Fig. 11 (b) and (c)). Given that the observed cracking pathways correspond to the lateral views of QC fracture surfaces, which are said to be responsible for the 10~20 times FCG acceleration (Fig. 6), the change in dislocation structure seems to be a natural consequence because the cumulative plastic strain in CPZ would accordingly be reduced to 1/10~1/20 despite the tests were conducted under the same ΔK. In other words, the crack promptly passes through CPZ before the final cellular state of the substructure development is reached, an inevitable outcome whatever underlying microscale mechanisms are responsible for the fast crack propagation under the influence of hydrogen.

In S55C steel that is slightly harder than S25C steel (Table 1), the CPZ size by Eq. (2) is ≈ 0.9 mm. The crack passage through CPZ in air resulted in the developed sub-grain microstructure (Fig. 10 (d)). Although these sub-grains formed within the inner-ferrite layers of pearlite no longer exhibit an equiaxed morphology, their bamboo-like appearance is not specific to our experiments. Similar structures have already been uncovered in low-cycle fatigue tests using smooth specimens of fully-eutectoid railway steels [63]. Such a particular configuration of sub-grains (or dislocation cells) is due to the intragranular-scale anisotropy of ferrite/cementite lamellar structure where the hard cementite platelets serve as impenetrable obstacles for the lateral motion of dislocations [64]. The bamboo-like sub-grains are observable when the inter-lamellar spacing is relatively large (*e.g.*, > 200 nm) and/or the applied plastic strain amplitude is sufficiently high [63].

Upon the assumption that the bamboo-like sub-grains and the associated KAM distributions are the principal indicators of the slow (*i.e.*, order of 10^{-7} m/cycle (Fig. 2)) crack propagation in S55C steel in air, it is worth noticing their similarities/dissimilarities with the substructures formed around the afore-mentioned two types of cracking pathways related to pearlite in hydrogen - PT and PD. Notably, the PT fracture (Fig. 10 (e) and Fig. 11 (e)) accompanied by the pronounced KAM and sub-grains development, which was not smaller than that around the pearlite-transecting crack in air. This fact invokes that the lamellar structure aligned nearly perpendicular to the crack plane might retain its significant resistance to the crack growth even under the presence of hydrogen, thus suppressing the onset of catastrophic FCG acceleration. A completely different picture is seen in the case of the PD-dominated fracture process, wherein neither recognizable KAM increase nor the formation of sub-grains/dislocation cells was found out even at the very intimate proximity to the crack edge (Fig. 10 (f) and Fig. 11 (f)). This observation reflects a high velocity and brittle nature of PD-type cracking in a way similar to QC in ferrite. Namely, the PD adversely contributes to the FCG rate enhancement in cooperation with QC, specifically when the pressure of hydrogen gas was 90 MPa, where the fraction of planar facets on the fracture surface was sizeable (Fig. 7 (b)). All these discussions support the previous hypothesis that arose at the end of Section 4.1: the mutually conflicting roles of PT and PD to respectively interfere and facilitate the extent of HA-FCG.

4.4 Dual roles of pearlite to interfere/facilitate the extent of HA-FCG

4.4.1 Crack propagation transecting the ferrite/cementite lamellar

As pointed out in Section 1, the existence of axially-aligned pearlite lamellar has been believed to rationalize the known prominent resistance to HE of cold drawn eutectoid steels [26,36]: fibrous cementite colonies act as obstacles impeding the HE-crack tending to propagate laterally to the loading direction. Despite the thin inner layers of pearlitic-ferrite may still be HE-prone, the cementite phase potentially remains immune to HE. This presumption is strongly supported by the numeric calculations showing that the occlusivity of hydrogen in pure Fe_3C is significantly low as compared with that in ferrite [35]. Indeed, the sluggish crack propagation when the crack grows toward the stacking direction of lamellae (I) (*c.f.* the situation illustrated in Fig. 10 (e)) has experimentally been demonstrated by Tomatsu et al. *via* nano-mechanical microcantilever bending tests in a SEM [36]. The same explanation can be applied to the FCG case observed in the present work when the well-developed self-organized deformation substructures evolved around the PT-type crack (Fig. 10 (e)). Furthermore, even when the lamellar stacking direction is aligned parallel to the line of crack-front (II), their study showed that the appreciable cracking resistance was possible, albeit its extent was slightly lesser compared to the case (I) [36]. In practice, the suppression of HA-FCG by pearlite in the hot-rolled carbon steels potentially stems from the synergy of these two scenarios (I) and (II) as well as their mixed mode. The evidence of their collective operation appeared on the randomly oriented, pearlite-induced stripe patterns on the fracture surfaces, particularly in 0.7 MPa hydrogen gas (Fig. 7 (c)).

Nonetheless, a contradictory result was reported in the research performed by the authors earlier [38] using tensile testing of similar carbon steels. It was shown that axially aligned pearlite advanced the loss of tensile ductility and exerted a rather detrimental effect on the mechanical performance in 95 MPa hydrogen gas. During monotonic loading, pearlite grains seemed to act as a preferential nucleation site for hydrogen-induced micro-cracks, leading to the shortened elongation to failure with an increase in f_P. This tensile HE-crack nucleation inside the pearlitic phase stemmed from the strain-controlled, shearing-off process occurring on the grain size scale along the maximum shear stress direction (*i.e.*, inclined almost 45° to the tensile axis). A microscopic mechanism of this process comprises localized-slip in pearlitic-ferrite assisted by hydrogen and subsequent fragmentation of fibrous cementite platelets [38]. Similarly, the pearlite-shearing was also confirmed to accelerate tensile fracture in the circumferentially-notched or fatigue pre-cracked round-bar specimens, where large-scale plastic deformation takes place at the roots of stress-concentrators [65]. Yu et al. recently investigated the HE-sensitivity of eutectoid steels as a function of pearlite inter-lamellar spacings ranging from 160 to 230 nm. They found that the ductility loss related to pearlite-shearing becomes more pronounced with the increasing distance between lamellae [37]. Since the lamellar spacing of presently examined carbon steels was of 0.2~1.2 μm, thus exceeding the range of materials tested in [37], more significant pearlite-shearing can be expected, although the images provided in Fig. 10 (b) and (c) do no support it. The absence of substantial pearlite-shearing during the FCG process can be attributed to the insufficiency of the strain level [65] and the non-uniform distribution of strains in the crack-tip-contacting pearlite grains within the presently examined ΔK range. As calculated by Eq. (2), the size of CPZ in the two carbon steels at ΔK = 25 MPa·m$^{1/2}$ was the order of 1 mm, which means that there are at least several grains inside CPZ which are supposed to be deformed plastically. Nevertheless, our previous study showed that more than 10% tensile strain is required to initiate shear cracking in pearlite during monotonic loading in hydrogen gas [38]. Even though the CPZ size was estimated from the simplified assumptions standing behind Eq.(2) based merely on the average yield stress of the ferrite-pearlite mixture, the zone subjected to a relatively large strain amplitude (> 10%) might be confined only to the extreme proximity of the crack-tip (*e.g.*, a few micrometers, which is by far smaller than the pearlite grain size), if one considers the hard nature of pearlite and high work-hardening ability of pearlite-rich microstructure at an early stage of the plastic deformation [38,66]. Indeed, the extent of the zone with high KAM values was correspondingly restricted to a distance less than 10 μm from the crack (Fig. 9 and Fig. 10)). Under such a circumstance, the shear cracking by which the crack instantaneously transects the encountered pearlite grains is not feasible. Moreover, while the coalescence of discrete pearlite cracks plays a key role to trigger HE in tensile tests [38], it is improbable for FCG, wherein the propagation of one main crack governs the fracture process.

4.4.2 Crack propagation delaminating the ferrite/cementite lamellar

Finally, the discussion in this section is centered around the delamination-type fracture along ferrite/cementite interfaces (*i.e.*, PD) that showed up as one of the two predominant failure modes and contributed to the FCG acceleration by counteracting the positive impact of PT in hydrogen gas (Fig. 7 (d) and Fig. 10 (c)). Intriguingly, the PD was not identified in our previous tensile testing [38]. This disparity can be ascribed to the difference in the stress level that the interface experiences during different modes of loading: the maximum stress in the tensile tests was no more than a few hundred MPa [38], whereas that at a sharp crack-tip it is much larger owing to the geometrical stress concentration and the plastic constraint under stress triaxiality. McEniry et al. investigated the hydrogen effect on the properties of perfectly coherent ferrite/cementite interface using *ab*-initio atomistic simulations [35]. It was demonstrated that the interface acts as a stable trapping site for hydrogen atoms in accord with the available experimental results [24,29,54]. Concurrently, the same authors have shown that trapped hydrogen considerably reduces the binding energy of the interfaces, giving rise to a premature debonding between the ferrite and cementite layers under the application of normal stress 10~20% lower than the fracture stress in the absence of hydrogen. In a simple term, their finding is consistent with the hydrogen-enhanced decohesion (HEDE) hypothesis, which was originally proposed to account for the reduction in inter-atomic cohesive force along the normal grain boundaries by hydrogen segregation [67,68]. Assuming that the same hypothesis can be applied to interphase boundaries in the present materials, the brittle delamination can selectively take place at the pearlite lamellar aligned perpendicularly to the loading direction where the normal stress component with respect to the lamellar plane is maximum (Fig. 12 (b)). The greater frequency of PD in 90 MPa hydrogen gas than at 0.7 MPa (Fig. 7 (a) and (b)) is also an acceptable outcome because the reduction in atomistic cohesion is a positive function of the total amount of occluded hydrogen [67,68] that determines local hydrogen concentration at the interface trap site [69].

Another possible contributing factor for the interface debonding is the prior deformation of the eventually-fractured pearlite grains before the crack-tip passage. Under the present ΔK level corresponding to the stabilized HA-FCG regime (*i.e.*, around 25 $\mathrm{MPa \cdot m^{1/2}}$) in which both the CPZ size (0.9 mm) and grain size (20~50 μm) are substantially greater than the da/dN values (order of 10^{-6} m/cycle, Fig. 2 (b)), a certain amount of dislocation could be accumulated at the phase boundary between ferrite and cementite in the pearlite grains located inside CPZ as was indeed inferred from the inset in Fig. 11 (f). These interface dislocations are known to be introducible even at a few % strain [70,71], stemming from the dislocation nucleation from the interface itself or statistical trapping of other dislocations which have swept out the inner-ferrite layers then encountered the impenetrable phase boundaries [63,70–72]. In the past studies utilizing thermal desorption spectroscopy (TDS) as a tool to detect the hydrogen state, an abnormal high temperature (300~400 K) desorption peak was discovered only when the pearlite structure was plastically deformed before the TDS measurements [24,25,32,37]. This fact was attributed to the supplemental hydrogen firmly trapped at the interfacial defects such as dislocations or vacancies, and they are deemed to be no longer diffusible at ambient temperature [25,32]. Ultimately, the interface dislocations and other defects further enhance hydrogen trapping capability, thereby assist hydrogen accumulation at the phase boundaries [25,37]. This further contributes to the reduction in interfacial cohesion, making the interfaces the weakest links for the crack to grow along as long as mechanical conditions of microstructural inhomogeneity do not force the crack to deviate from the easy path.

Combining all the preceding discussions and findings of the present work, the development of ferrite-pearlite carbon steels with excellent resistance to HA-FCG relies on a strategy that proactively increases the fraction of pearlite and simultaneously controls the microstructure so as to avoid the formation of pearlite lamellar planes lying perpendicularly to the practical loading axis. The methodologies for accomplishing the latter aim in pro-eutectoid steels have yet to be established, though a directed lamellar structure has been achieved for purpose in fully-eutectoid steel *via* utilization of the unidirectional transformation [73]. However, the lowering of the latent fracture toughness as well as the increasing tensile HE-sensitivity of the pearlite-rich materials are the possible critical drawbacks particularly when the lamellar spacing of pearlite is relatively coarse [37,38,74,75]. Thus, these other detrimental factors should be took into account for a more comprehensively optimized steel design, a consideration on which is a task of our ongoing research.

5. Conclusions

Fatigue crack growth (FCG) tests of two hot-rolled carbon steels with different carbon contents (0.25 and 0.54%) were performed in 0.7 and 90 MPa gaseous hydrogen, in order to clarify the impact of pearlite on the hydrogen-related acceleration behavior of the FCG. Detailed fractography combined with the deformation microstructural characterizations on the cross-sectional crack-wakes were supplementarily employed for the mechanism elucidation of the FCG rate changes owing to the altering pearlite volume fractions. The main conclusions are summarized as follows.

1. Increasing carbon content from 0.25 to 0.54% and the concomitant increasing volume fraction of pearlite from 31 to 69% effectively mitigated the magnitude of hydrogen-assisted (HA-) FCG up to of 40~70%. The effect was more pronounced at low hydrogen pressure. The beneficial influence of the increased volume fraction of pearlite was observed for all the test frequencies ranging between 0.01 and 1 Hz in the present experiments.
2. The fractographic character of pearlite in the presence of hydrogen was divided into two types: striated distinction evidencing the tearing of pearlite lamellar aligned perpendicular to the global crack-plane (PT) and planer facets originating from the delamination along ferrite/cementite

interfaces lying nearly parallel to the crack-plane (PD). The appearance of the latter feature was particularly pronounced at the higher hydrogen pressure.

3. The plastic wake region along the crack path corresponding to the PT fracture is featured by a well-organized dislocation sub-structure, which are formed in response of high cyclic plastic strains in the pearlitic inter-lamellae regions, and which are required considerable plastic work ahead of the crack tip. This caused remarkable retardation of FCG as the crack front encountered favorably oriented cementite platelets acting as barriers intermittently arresting the fatigue crack. No signatures of well-developed dislocation structures existed around the crack when it grew by the PD mechanism, indicating the rapid and brittle nature of ferrite/cementite interface cracking *via* hydrogen-enhanced atomistic debonding.
4. Based on the above findings, it is envisaged that the experimentally identified superior HA-FCG resistance of pearlite-rich steel relies primarily on the operation of the PT mechanism. The probability of this mechanism to occur depends on the volume fraction and microstructure of pearlite, providing possible routes for metallurgists to further tailor the ferrite-pearlite microstructure towards optimization of its response to hydrogen-induced detrimental effects on FCG. On the other hand, PD cracking counteracted and partially compromised the positive influence of PT, thus acting as one of the constituents responsible for the degradation in the material's performance, especially at high hydrogen gas pressure.

Acknowledgement

This work was partially supported by Research Council of Norway, Project No. 294739, Safe Pipelines for Hydrogen Transport (HyLINE) and Project No. 309378, Japan-Norway Partnership on Hydrogen-Materials Interaction (H2NINJA).

References

[1] Barthélémy H. Hydrogen storage – Industrial prospectives. Int J Hydrogen Energy 2012;37:17364–72. https://doi.org/10.1016/j.ijhydene.2012.04.121.

[2] Djukic MB, Bakic GM, Zeravcic VS, Sedmak A, Rajicic B. Hydrogen embrittlement of industrial components: Prediction, prevention, and models. Corrosion 2016;72:943–61. https://doi.org/10.5006/1958.

[3] Takai K, Shoda H, Suzuki H, Nagumo M. Lattice defects dominating hydrogen-related failure of metals. Acta Mater 2008;56:5158–67. https://doi.org/10.1016/j.actamat.2008.06.031.

[4] Michler T, Naumann J. Microstructural aspects upon hydrogen environment embrittlement of various bcc steels. Int J Hydrogen Energy 2010. https://doi.org/10.1016/j.ijhydene.2009.10.092.

[5] Birenis D, Ogawa Y, Matsunaga H, Takakuwa O, Yamabe J, Prytz Ø, et al. Hydrogen-assisted crack propagation in α-iron during elasto-plastic fracture toughness tests. Mater Sci Eng A 2019;756:396–404. https://doi.org/10.1016/j.msea.2019.04.084.

[6] Koyama M, Akiyama E, Tsuzaki K, Raabe D. Hydrogen-assisted failure in a twinning-induced plasticity steel studied under in situ hydrogen charging by electron channeling contrast imaging. Acta Mater 2013;61:4607–18. https://doi.org/10.1016/j.actamat.2013.04.030.

[7] Nanninga N, Slifka a., Levy Y, White C. A review of fatigue crack growth for pipeline steels exposed to

hydrogen. J Res Natl Inst Stand Technol 2010;115:437. https://doi.org/10.6028/jres.115.030.

[8] Ogawa Y, Matsunaga H, Yamabe J, Yoshikawa M, Matsuoka S. Fatigue limit of carbon and Cr Mo steels as a small fatigue crack threshold in high-pressure hydrogen gas. Int J Hydrogen Energy 2018;43:20133–42. https://doi.org/10.1016/j.ijhydene.2018.09.026.

[9] Matsunaga H, Yoshikawa M, Kondo R, Yamabe J, Matsuoka S. Slow strain rate tensile and fatigue properties of Cr–Mo and carbon steels in a 115 MPa hydrogen gas atmosphere. Int J Hydrogen Energy 2015;40:5739–48. https://doi.org/10.1016/j.ijhydene.2015.02.098.

[10] Kawakami R, Kubota K, Matsunaga H. Rotating Bending Fatigue Property of SCM435 during Electrochemical Hydrogen Charging. J Japan Inst Met Mater 2020;84:92–8. https://doi.org/10.2320/jinstmet.JB201901.

[11] Wan D, Deng Y, Meling JIH, Alvaro A, Barnoush A. Hydrogen-enhanced fatigue crack growth in a single-edge notched tensile specimen under in-situ hydrogen charging inside an environmental scanning electron microscope. Acta Mater 2019;170:87–99. https://doi.org/10.1016/j.actamat.2019.03.032.

[12] Matsunaga H, Takakuwa O, Yamabe J, Matsuoka S. Hydrogen-enhanced fatigue crack growth in steels and its frequency dependence. Philos Trans R Soc A Math Phys Eng Sci 2017;375:20160412. https://doi.org/10.1098/rsta.2016.0412.

[13] Somerday BP, Sofronis P, Nibur KA, San Marchi C, Kirchheim R. Elucidating the variables affecting accelerated fatigue crack growth of steels in hydrogen gas with low oxygen concentrations. Acta Mater 2013;61:6153–70. https://doi.org/10.1016/j.actamat.2013.07.001.

[14] Ogawa Y, Umakoshi K, Nakamura M, Takakuwa O, Matsunaga H. Hydrogen-assisted, intergranular, fatigue crack-growth in ferritic iron: Influences of hydrogen-gas pressure and temperature variation. Int J Fatigue 2020;140:105806. https://doi.org/10.1016/j.ijfatigue.2020.105806.

[15] Yamabe J, Yoshikawa M, Matsunaga H, Matsuoka S. Hydrogen trapping and fatigue crack growth property of low-carbon steel in hydrogen-gas environment. Int J Fatigue 2017;102:202–13. https://doi.org/10.1016/j.ijfatigue.2017.04.010.

[16] Takakuwa O, Ogawa Y, Okazaki S, Nakamura M, Matsunaga H. A mechanism behind hydrogen-assisted fatigue crack growth in ferrite-pearlite steel focusing on its behavior in gaseous environment at elevated temperature. Corros Sci 2020:108558. https://doi.org/10.1016/j.corsci.2020.108558.

[17] Ronevich JA, Somerday BP, San Marchi CW. Effects of microstructure banding on hydrogen assisted fatigue crack growth in X65 pipeline steels. Int J Fatigue 2015;82:497–504. https://doi.org/10.1016/j.ijfatigue.2015.09.004.

[18] Macadre A, Artamonov M, Matsuoka S, Furtado J. Effects of hydrogen pressure and test frequency on fatigue crack growth properties of Ni-Cr-Mo steel candidate for a storage cylinder of a 70MPa hydrogen filling station. Eng Fract Mech 2011;78:3196–211. https://doi.org/10.1016/j.engfracmech.2011.09.007.

[19] Peral LB, Zafra A, Blasón S, Rodríguez C, Belzunce J. Effect of hydrogen on the fatigue crack growth rate of quenched and tempered CrMo and CrMoV steels. Int J Fatigue 2019;120:201–14. https://doi.org/10.1016/j.ijfatigue.2018.11.015.

[20] Birenis D, Ogawa Y, Matsunaga H, Takakuwa O, Yamabe J, Prytz Ø, et al. Interpretation of hydrogen-assisted fatigue crack propagation in BCC iron based on dislocation structure evolution around the crack wake. Acta Mater 2018;156:245–53. https://doi.org/10.1016/j.actamat.2018.06.041.

[21] Ogawa Y, Birenis D, Matsunaga H, Takakuwa O, Yamabe J, Prytz Ø, et al. The role of intergranular fracture on hydrogen-assisted fatigue crack propagation in pure iron at a low stress intensity range. Mater Sci Eng A 2018;733:316–28. https://doi.org/10.1016/j.msea.2018.07.014.

[22] Suresh S. Further remarks on the micromechanisms of fatigue crack growth retardation following overloads. Eng Fract Mech 1985;21:1169–70. https://doi.org/10.1016/0013-7944(85)90175-4.

[23] Korda AA, Mutoh Y, Miyashita Y, Sadasue T, Mannan SL. In situ observation of fatigue crack retardation in banded ferrite–pearlite microstructure due to crack branching. Scr Mater 2006;54:1835–40. https://doi.org/10.1016/j.scriptamat.2006.02.025.

[24] Kim JS, Lee YH, Lee DL, Park K-T, Lee CS. Microstructural influences on hydrogen delayed fracture of high strength steels. Mater Sci Eng A 2009;505:105–10. https://doi.org/10.1016/j.msea.2008.11.040.

[25] Takai K, Watanuki R. Hydrogen in Trapping States Innocuous to Environmental Degradation of High-strength Steels. ISIJ Int 2003;43:520–6. https://doi.org/10.2355/isijinternational.43.520.

[26] Fujita T, Yamada Y. Stress Corrosion Cracking and Hydrogen Embrittlement of Iron Base Alloys. NACE 5, 1977, p. 736.

[27] Marandet B. Stress corrosion cracking and hydrogen embrittlement of iron base alloys. NACE 5, 1977.

[28] Toribio J. HELP versus HEDE in progressively cold-drawn pearlitic steels: Between Donatello and Michelangelo. Eng Fail Anal 2018;94:157–64. https://doi.org/10.1016/j.engfailanal.2018.07.026.

[29] Hagi H. Effect of Interface between Cementite and Ferrite on Diffusion of Hydrogen in Carbon Steels. Mater Trans JIM 1994;35:168–73. https://doi.org/10.2320/matertrans1989.35.168.

[30] Kawakami K, Matsumiya T. Ab-initio Investigation of Hydrogen Trap State by Cementite in bcc-Fe. ISIJ Int 2013;53:709–13. https://doi.org/10.2355/isijinternational.53.709.

[31] Chida T, Kosaka M, Kubota M, Tarui T, Omura T. Effects of Drawn Strain and Aging Temperature on Critical Diffusible Hydrogen Content and Absorbed Hydrogen Content in Pearlitic Steel Wires. Tetsu-to-Hagane 2019;105:655–63. https://doi.org/10.2355/tetsutohagane.TETSU-2019-002.

[32] Doshida T, Takai K. Dependence of hydrogen-induced lattice defects and hydrogen embrittlement of cold-drawn pearlitic steels on hydrogen trap state, temperature, strain rate and hydrogen content. Acta Mater 2014;79:93–107. https://doi.org/10.1016/j.actamat.2014.07.008.
[33] Costa JE, Thompson AW. Hydrogen Cracking in Nominally Pearlitic 1045 Steel. Metall Trans A 1982;13:1315–8. https://doi.org/10.1007/BF02645516.
[34] Toribio J, Lancha AM, Elices M. The tearing topography surface as the zone associated with hydrogen embrittlement processes in pearlitic steel. Metall Trans A 1992;23:1573–84. https://doi.org/10.1007/BF02647339.
[35] McEniry EJ, Hickel T, Neugebauer J. Ab initio simulation of hydrogen-induced decohesion in cementite-containing microstructures. Acta Mater 2018;150:53–8. https://doi.org/10.1016/j.actamat.2018.03.005.
[36] Tomatsu K, Amino T, Chida T, Uji S, Okonogi M, Kawata H, et al. Anisotropy in Hydrogen Embrittlement Resistance of Drawn Pearlitic Steel Investigated by *in-situ* Microbending Test during Cathodic Hydrogen Charging. ISIJ Int 2018;58:340–8. https://doi.org/10.2355/isijinternational.ISIJINT-2017-461.
[37] Yu S-H, Lee S-M, Lee S, Nam J-H, Lee J-S, Bae C-M, et al. Effects of lamellar structure on tensile properties and resistance to hydrogen embrittlement of pearlitic steel. Acta Mater 2019;172:92–101. https://doi.org/10.1016/j.actamat.2019.04.040.
[38] Ogawa Y, Hino M, Nakamura M, Matsunaga H. Pearlite-driven surface-cracking and associated loss of tensile ductility in plain-carbon steels under exposure to high-pressure gaseous hydrogen. Int J Hydrogen Energy 2021;46:6945–59. https://doi.org/10.1016/j.ijhydene.2020.11.137.
[39] Abbaschian R, Abbaschian L. Physical Metallurgy Principles. 4th ed. Cl-Engineering; 2008.
[40] ASTM. E647-08-1. Standard test method for measurement of fatigue crack growth rates. West Conshohocken: ASTM International; 2010.
[41] Wei R, Landes J. Correlation between sustained-load and fatigue crack growth in high-strength steels. Mater Res Stand 1969;9:25–46.
[42] Yamabe J, Matsumoto T, Matsuoka S, Murakami Y. A new mechanism in hydrogen-enhanced fatigue crack growth behavior of a 1900-MPa-class high-strength steel. Int J Fract 2012;177:141–62. https://doi.org/10.1007/s10704-012-9760-9.
[43] Sun Z, Moriconi C, Benoit G, Halm D, Henaff G. Fatigue Crack Growth under High Pressure of Gaseous Hydrogen in a 15-5PH Martensitic Stainless Steel: Influence of Pressure and Loading Frequency. Metall Mater Trans A 2013;44:1320–30. https://doi.org/10.1007/s11661-012-1133-5.
[44] Zaefferer S, Elhami NN. Theory and application of electron channelling contrast imaging under controlled diffraction conditions. Acta Mater 2014;75:20–50. https://doi.org/10.1016/j.actamat.2014.04.018.
[45] Macadre A, Nakada N, Tsuchiyama T, Takaki S. Critical grain size to limit the hydrogen-induced ductility drop in a metastable austenitic steel. Int J Hydrogen Energy 2015;40:10697–703. https://doi.org/10.1016/j.ijhydene.2015.06.111.
[46] Koyama M, Wang H, Verma VK, Tsuzaki K, Akiyama E. Effects of Mn Content and Grain Size on Hydrogen Embrittlement Susceptibility of Face-Centered Cubic High-Entropy Alloys. Metall Mater Trans A 2020;51:5612–6. https://doi.org/10.1007/s11661-020-05966-z.
[47] Matsuoka S, Matsunaga H, Yamabe J, Hamada S, Iijima T. Various strength properties of SCM435 and SNCM439 low-alloy steels in 115 MPa hydrogen gas and proposal of design guideline. Trans JSME (in Japanese) 2017;83:17-00264-17–00264. https://doi.org/10.1299/transjsme.17-00264.
[48] Martin ML, Fenske JA, Liu GS, Sofronis P, Robertson IM. On the formation and nature of quasi-cleavage fracture surfaces in hydrogen embrittled steels. Acta Mater 2011;59:1601–6. https://doi.org/10.1016/j.actamat.2010.11.024.
[49] Merson ED, Myagkikh PN, Poluyanov VA, Merson DL, Vinogradov A. Quasi-cleavage hydrogen-assisted cracking path investigation by fractographic and side surface observations. Eng Fract Mech 2019;214:177–93. https://doi.org/10.1016/j.engfracmech.2019.04.042.
[50] Anderson TL. Fracture mechanics fundamentals and applications. CRC Press 2017.
[51] Takahashi Y, Nishikawa H, Oda Y, Noguchi H. Microscopic characterization of hydrogen-induced quasi-brittle fatigue fracture in low-strength carbon steel. Mater Lett 2010;64:2416–9. https://doi.org/10.1016/j.matlet.2010.08.019.
[52] Hinotani S, Ohmori Y, Terasaki F. Hydrogen crack initiation and propagation in pure iron single crystal. Mater Sci Technol 1994;10:141–8. https://doi.org/10.1179/mst.1994.10.2.141.
[53] Kimura A, Kimura H. Hydrogen embrittlement in high purity iron single crystals. Mater Sci Eng 1986;77:75–83. https://doi.org/10.1016/0025-5416(86)90355-1.
[54] Jeng HW, Chiu LH, Johnson DL, Wu JK. Effect of pearlite morphology on hydrogen permeation, diffusion, and solubility in carbon steels. Metall Trans A 1990;21:3257–9. https://doi.org/10.1007/BF02647319.
[55] Awatani J, Katagiri K, Nakai H. Dislocation structures around propagating fatigue cracks in iron. Metall Trans A 1978;9:111–6. https://doi.org/10.1007/BF02647179.
[56] Purcell AH, Weertman J. Transmission electron microscopy of the crack tip region of fatigued copper single crystals. Metall Trans 1973;4:349–53. https://doi.org/10.1007/BF02649636.
[57] Grosskreutz J., Shaw G. Fine subgrain structure adjacent to fatigue cracks. Acta Metall 1972;20:523–8. https://doi.org/10.1016/0001-6160(72)90008-9.
[58] Roven HJ, Nes E. Cyclic deformation of ferritic steel—II. Stage II crack propagation. Acta Metall Mater

1991;39:1735–54. https://doi.org/10.1016/0956-7151(91)90142-N.

[59] Taniguchi T, Kaneko Y, Hashimoto S. ECCI observations of dislocation structures around fatigue cracks in ferritic stainless steel single crystals. IOP Conf Ser Mater Sci Eng 2009;3:012020. https://doi.org/10.1088/1757-899X/3/1/012020.

[60] Kaneko Y, Ishikawa M, Hashimoto S. Dislocation structures around crack tips of fatigued polycrystalline copper. Mater Sci Eng A 2005;400–401:418–21. https://doi.org/10.1016/j.msea.2005.02.080.

[61] Purcell AH, Weertman J. Crack tip area in fatigued copper single crystals. Metall Trans 1974;5:1805–9. https://doi.org/10.1007/BF02644144.

[62] Rice JR. Mechanics of Crack Tip Deformation and Extension by Fatigue. Fatigue Crack Propag., 100 Barr Harbor Drive, PO Box C700, West Conshohocken, PA 19428-2959: ASTM International; n.d., p. 247-247–65. https://doi.org/10.1520/STP47234S.

[63] Sunwoo H, Fine ME, Meshii M, Stone DH. Cyclic deformation of pearlitic eutectoid rail steel. Metall Trans A 1982;13:2035–47. https://doi.org/10.1007/BF02645949.

[64] Li S, Yip TH, Ramanujan R V., Liang MH. Insitu TEM studies of the mechanisms of crack nucleation and propagation in fully lamellar microstructures. Mater Sci Technol 2003;19:902–6. https://doi.org/10.1179/026708303225004378.

[65] Enos DG, Scully JR. A critical-strain criterion for hydrogen embrittlement of cold-drawn, ultrafine pearlitic steel. Metall Mater Trans A 2002;33:1151–66. https://doi.org/10.1007/s11661-002-0217-z.

[66] Karlsson B, Lindén G. Plastic deformation of ferrite—pearlite structures in steel. Mater Sci Eng 1975;17:209–19. https://doi.org/10.1016/0025-5416(75)90232-3.

[67] Oriani RA, Josephic PH. Equilibrium aspects of hydrogen-induced cracking of steels. Acta Metall 1974;22:1065–74. https://doi.org/10.1016/0001-6160(74)90061-3.

[68] Wang S, Martin ML, Robertson IM, Sofronis P. Effect of hydrogen environment on the separation of Fe grain boundaries. Acta Mater 2016;107:279–88. https://doi.org/10.1016/j.actamat.2016.01.067.

[69] Oriani R. The diffusion and trapping of hydrogen in steel. Acta Metall 1970;18:147–57. https://doi.org/10.1016/0001-6160(70)90078-7.

[70] Dollar M, Bernstein IM, Thompson AW. Influence of deformation substructure on flow and fracture of fully pearlitic steel. Acta Metall 1988;36:311–20. https://doi.org/10.1016/0001-6160(88)90008-9.

[71] Dollar M, Bernstein IM, Daeubler M, Thompson AW. The effect of cyclic loading on the dislocation structure of fully pearlitic steel. Metall Trans A 1989;20:447–51. https://doi.org/10.1007/BF02653924.

[72] Porter DA, Easterling KE, Smith GDW. Dynamic studies of the tensile deformation and fracture of pearlite. Acta Metall 1978;26:1405–22. https://doi.org/10.1016/0001-6160(78)90156-6.

[73] Mellor BG, Edmonds D V. Unidirectional transformation of Fe-0.8C-Co alloys: Part I. Process per structure relationships and the significance of pearlite interlamellar spacing measurements. Metall Trans A 1977;8:763–71. https://doi.org/10.1007/BF02664786.

[74] Gladshtein LI, Larionova NP, Belyaev BF. Effect of ferrite-pearlite microstructure on structural steel properties. Metallurgist 2012;56:579–90. https://doi.org/10.1007/s11015-012-9619-3.

[75] Rosenfield AR, Hahn GT, Embury JD. Fracture of steels containing pearlite. Metall Mater Trans B 1972;3:2797–804. https://doi.org/10.1007/BF02652845.